A pH-responsive hyaluronic acid nano-vehicle co-encapsulating doxorubicin and all-trans retinoic acid for the inhibition of hepatic stellate cell-induced tumor growth and metastasis

QIAO LU[1,2*], XUEYANG GONG[1*], GUANGTAO JIA[1*], JINGLIANG WU[2], SIWEI LIU[1], KE SONG[1] and GUIXIANG TIAN[1]

[1]Department of Life Science and Technology, Weifang Medical University, Weifang, Shandong 261053; [2]Department of Nursing, Weifang University of Science and Technology, Weifang, Shandong 262700, P.R. China

Received December 29, 2022; Accepted May 15, 2023

DOI: 10.3892/mmr.2023.13029

Abstract. All-trans retinoic acid (ATRA) has been implicated in the differentiation of hepatic stellate cells (HSCs). In the present study, the liver-targeting hyaluronic acid micelles (ADHG) were prepared for co-delivery of ATRA and doxorubicin (DOX) to block the HSC-hepatoma interrelation. To simulate the tumor microenvironment, an *in vitro* dual-cell model and an *in vivo* co-implantation mouse model were established for anticancer studies. The experimental methods involved the MTT assay, wound-healing assay, cellular uptake, flow cytometry and and *in vivo* antitumor study. The results revealed that the HSCs in the research models notably promoted tumor proliferation and migration. Furthermore, ADHG were readily internalized by cancer cells and HSCs simultaneously, and widely distributed in cancer regions. The *in vivo* antitumor studies demonstrated that ADHG could notably decrease HSC activation and extracellular matrix deposition, as well as constrain tumor growth and metastasis. Therefore, ATRA could facilitate DOX-induced anti-proliferation and anti-metastasis effects, and ADHG are a promising nano-sized formulation for the combination therapy of hepatocellular carcinoma.

Correspondence to: Professor Jingliang Wu, Department of Nursing, Weifang University of Science and Technology, 1299 Jinguang Road, Shouguang, Weifang, Shandong 262700, P.R. China
E-mail: jlwu2008@163.com

*Contributed equally

Abbreviations: ADH, ATRA/DOX-sHA; ADHG, ATRA/DOX-sHA-GA; ATRA, all-trans retinoic acid; CFSE, 5(6)-carboxyfluorescein diacetate succinimidyl ester; CLMS, confocal laser microscope; DH, DOX-sHA; DHG, DOX-sHA-GA; DiR, 1,1-dioctadecyl-3,3,3,3-tetramethylindotricarbocyanine iodide; DL, drug-loading rate; DOX, doxorubicin; ECM, extracellular matrix; EE, encapsulation efficiency rate; FCM, flow cytometry; GA, glycyrrhetinic acid; HA, hyaluronic acid; HCC, hepatocellular carcinoma; HSC, hepatic stellate cell; m-HSC, mouse HSC; NDDS, nano-sized drug delivery systems; sHA, sulfated HA; TME, tumor microenvironment; TEM, transmission electron microscope

Key words: all-trans retinoic acid, hepatic stellate cells, combination therapy, anti-hepatoma

Introduction

All-trans retinoic acid (ATRA) plays a vital role in the differentiation of hepatic stellate cells (HSCs) (1). In advanced liver fibrosis, HSCs are activated to shift from a quiescent phenotype into myofibroblasts expressing α-smooth muscle actin (α-SMA), a marker of activated hepatic stellate cells), in the absence of ATRA. The activation of HSCs is inhibited when extracellular ATRA levels increase (2-4). In the liver, ATRA binds to retinoic acid receptors β and α of HSCs to restrain the production of collagen fibers (5-7). A recent study revealed that ATRA can constrain HSC proliferation and extracellular matrix (ECM) deposition via the JNK-dependent NF-κB signaling pathway (8). Moreover, ATRA can enhance the effect of cisplatin by inducing the differentiation of tumor initiating cells and decreasing the chemoresistant subpopulations of hepatocellular carcinoma (HCC) cells (9).

HCC cells are located in a complex microenvironment in which stromal cells, including HSCs, endothelial cells and immune cells, participate in the development of tumors (10,11). Among them, HSCs can be activated by tumor cells. In the tumor microenvironment (TME), HSCs not only induce ECM deposition by producing type I collagen, but also secrete various factors, such as interleukin 6 (IL-6), IL-8 and monocyte chemoattractant protein-1, to induce cancer development (12-17). Hence, inhibition of HSC-induced tumor growth is an effective strategy for anti-HCC therapy. Considering that activated HSCs are located in the TME of HCC, it is possible that a combination therapy based on ATRA and chemotherapeutic drugs might display a synergistic anticancer therapeutic approach through HSCs redifferentiation and tumor apoptosis.

However, free drug formulations are limited in their clinical use due to systemic toxicity, short half-life and low solubility (18). Nano-sized drug delivery systems (NDDSs) have been demonstrated to be potential carriers for the

delivery of antitumor drugs (19,20). Compared with traditional formulations, NDDSs possess a lower systemic toxicity, longer circulation time in the blood and higher bioavailability. Moreover, nano-sized formulations can improve the selective solubility of insoluble drugs to tumor cells. Hyaluronic acid (HA), a natural polysaccharide, is abundantly present in the ECM and has non-toxic, non-immunogenic properties (21,22). High-molecular weight HA has been shown to inhibit tumor development, while a simple degradation process to low-molecular weight HA by hyaluronidase in the TME allows for the low-molecular weight HA to facilitate tumor migration (23). sHA (sulfated HA) has been previously synthesized by introducing sulphation to the-OH groups of HA polymers and used to block degradation by hyaluronidase, thus inhibiting the proliferation, motility and invasion of tumor cells (24,25). Amphiphilic conjugates based on HA polymers are self-assembled into nanoparticles composed of hydrophobic cores and hydrophilic shells (26,27). Moreover, drug-loaded HA nanoparticles specifically bind to CD44 receptors, which are highly expressed on activated HSCs, thereby enhancing the antitumor effect via CD44 receptor-mediated endocytosis (28,29). The use of drug-loaded HA nanoparticles has been demonstrated in cancer treatment, such as that of breast cancer, HCC and colorectal cancer (30-32).

In the present study, liver-targeting co-loaded HA nanoparticles (ADHG) were prepared to inhibit HSC-induced tumor proliferation and metastasis (Fig. 1A). To mimic the TME, an *in vitro* dual-cell research model and an *in vivo* co-implantation mouse model composed of stromal cells and cancer cells were established for antitumor studies. The anti-proliferation and the anti-migration effects of ADHG were evaluated against cancer cells alone and the dual-cell model. The drug distribution and the antitumor efficacy of ADHG was also investigated in co-implantation mice.

Materials and methods

Materials. ATRA was purchased from Shanghai Aladdin Biochemical Technology Co., Ltd. Doxorubicin (DOX), fluorescence probes 1,1-dioctadecyl-3,3,3,3-tetramethylindotricarbocyanine iodide (DiR), RPMI-1640 medium and the Calcein-AM/PI kit were obtained from Dalian Meilun Biology Technology Co., Ltd. Cell culture medium and H&E and Masson staining kit were acquired from Beijing Solarbio Science & Technology Co., Ltd. The 5(6)-carboxyfluorescein diacetate succinimidyl ester (CFSE) fluorescence dye was obtained from Abcam. Anhydrous ethanol and xylene were of analytical grade (Analytical Reagent; Red Label).

Cell lines and animals. Huh-7 cells (human HCC line; cat. no. 1101HUM-PUMC000679) were obtained from China Infrastructure of Cell Line Resources, Institute of Basic Medical Sciences, Chinese Academy of Medical Sciences. H22 (mouse HCC line; cat. no. GDC0091), LX-2 (human HSC line; cat. no. GPC0076) and m-HSC (mouse HSC line; cat. no. GPC0414) cells were purchased from the China Center for Type Culture Collection. Human-derived cells and mouse-derived cells were used for *in vitro* and *in vivo* experiments, respectively. A total of 80 female BALB/c mice (weight, 18 g; age, 6-8 weeks) were obtained from Jinan Pengyue Experimental Animal Breeding Co., Ltd.

Preparation and characterization of ADHG nanoparticles. The sHA is a polymer synthesized by grafting chlorosulfonic acid onto HA. Considering that sHA could inhibit hyaluronidase-induced HA degradation, sHA was used as the drug carrier in the present study. The DOX-sHA (DH) polymers were laboratory-made. DH and ATRA were dissolved in distilled water and anhydrous ethanol solution, respectively. The two solutions were mixed (final volumes, 10 ml) at different mass ratios of DH and ATRA (10:1, 5:1 and 2.5:1), followed by ultrasonication for 10 min (20 KHz) under ice water bath to prepare ATRA/DH (ADH) nanoparticles using a probe-type sonicator (VCX-750; Sonics Vibra-Cell™). To remove the unloaded ATRA, the mixed solution was dialyzed in distilled water using a dialysis bag (molecular weight cut-off, 3,500) at room temperature for 24 h. Subsequently, the obtained solutions were freeze-dried at -45˚C for further study. Similarly, ADHG nanoparticles were prepared by adding glycyrrhetinic acid (GA)-modified HA polymers to ADH solution and sonicated (20 KHz) in an ice water bath for 15 min. DOX-sHA-GA (DHG) nanoparticles were prepared by adding GA-modified HA polymer to DH solution and sonicated using the same method.

The average particle size of ADHG was detected by a Malvern Nano-ZS90 analyzer (33). The morphology of nanoparticles was observed using a transmission electron microscope (TEM; model no. HT7700; Hitachi High-Technologies Corporation). The stability of ADHG nanoparticles was examined in PBS solution (pH 7.4) or RPMI 1640 medium containing 10% fetal bovine serum (FBS; ExCell Bio) for 7 days. The ATRA content was calculated according to a standard curve, and the drug-loading rate (DL) and encapsulation efficiency rate (EE) of ATRA were measured using a UV spectrophotometer at 340 nm.

In vitro cytotoxicity. The *in vitro* dual-cell research model was established by mixing cancer cells and HSCs at a ratio of 5:1 (34). The MTT assay was then used to detect the cytotoxicity of ADHG. In brief, free ATRA, free DOX, DOX + ATRA, DH, ADH and ADHG solutions were added into the 96-well plates ($5x10^3$ cells/well) to achieve DOX concentrations ranging from 0.01 to 10 μg/ml and incubated for 48 h at 37˚C. Dimethyl sulfoxide was used to dissolve the purple formazan and cell viability was detected using a microplate reader at 490 nm. The experiment was repeated in triplicate. Similarly, a live/dead assay was performed using a Calcein-AM/PI kit (Meilun Biotechnology Co., Ltd.), and the images were obtained using a fluorescent microscope.

Wound-healing assay. To distinguish Huh-7 and LX-2 cells under a microscope, LX-2 cells were labeled with CFSE. The wound-healing assay was conducted using cancer cells and the dual-cell system (35). Prior to the assay, the cells were subjected to serum starvation (2% FBS) for 24 h in 37˚C. When the cells reached ~80% confluency in each well, the cells were scratched using a 200 μl pipette tip to form a wound area and subsequently treated with different drug

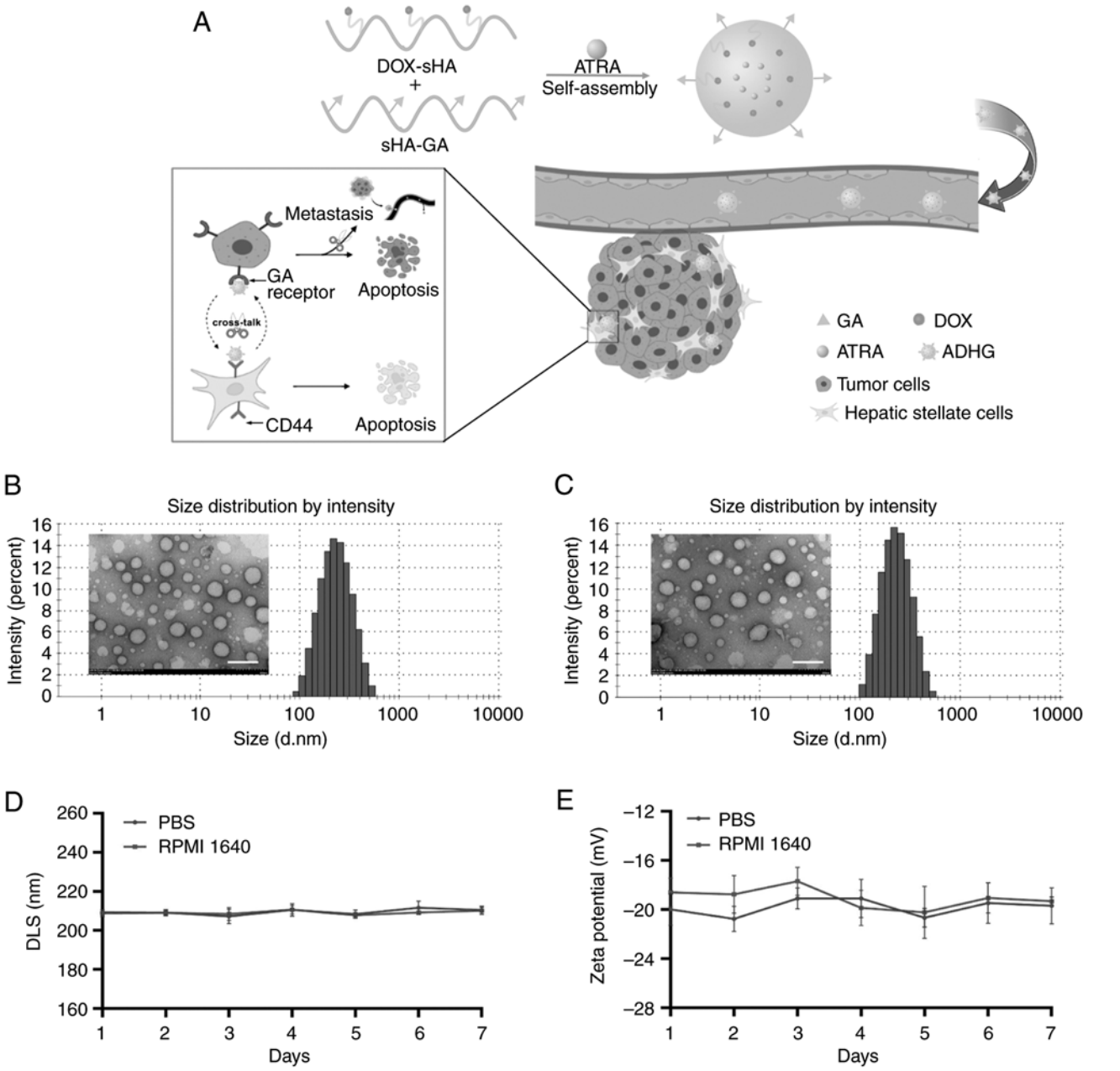

Figure 1. Illustration and characteristics of drug-loaded nanoparticles. (A) Design of the combination therapy. Transmission electron microscope images and particle sizes of (B) DOX-sHA-GA and (C) ATRA/DOX-sHA-GA (scale bar, 200 nm). (D and E) Stability of ADHG under physiological conditions within 7 days. (D) DLS and (E) Zeta potential. ADHG, ATRA/DOX-sHA-GA; DOX, doxorubicin; sHA, sulfated hyaluronic acid; GA, glycyrrhetinic acid; ATRA, all-trans retinoic acid; DLS, dynamic light scattering.

solutions of DOX, ATRA, DOX + ATRA, DH, ADH, ADHG (equivalent DOX, 2 μg/ml; ATRA, 1.47 μg/ml) for 24 h at 37˚C. The wound-healing images were observed with a Nikon fluorescence microscope, (Nikon eclipse Ti-S; Nikon Corporation), and the cell migration rate was analyzed by the edge-finding method using Image J 1.8.0 (National Institutes of Health).

Cellular uptake. The liver-targeting ability of ADHG was measured against Huh-7 cells and the dual-cell model *in vitro*. The cells were treated with DOX, DH and DHG (equivalent DOX, 10 μg/ml) for 3 h at 37˚C, followed by DAPI (1 μg/ml) staining for 10 min and observation using a confocal laser microscope (CLMS). The intracellular DOX fluorescence intensity was also examined using analyte reporter PE by flow cytometry (BD accuri c6 plus; BD Biosciences) and analyzed by FlowJo v10 (BD Biosciences).

In vivo drug distribution. The liver-targeting capacity of ADHG was also studied using an *in vivo* imaging system. An *in vivo* co-implantation model was established by subcutaneous injection of 0.2 ml of $2x10^6$ H22/m-HSC cells into the right flank, and DiR was loaded in DHG nanoparticles to evaluate drug distribution *in vivo*. The subcutaneous tumor-bearing mice were injected intravenously with 0.2 ml free DiR, DH + DiR and DHG + DiR (DiR; 4 mg/kg). *In vivo* fluorescent images were captured at different time points by the PerkinElmer IVIS Spectrum system.

Table I. Characterization of the different nanoparticle formulations.

DHG:ATRA	DLS, nm	PDI	ζ-Potential, mV	EE, %	DL, %
10:1	258.40±3.41	0.149±0.02	-18.01±0.55	84.85±7.18	7.71±0.65
5:1	211.95±2.61	0.110±0.01	-18.97±0.46	52.72±5.18	8.79±0.86
2.5:1	240.70±1.13	0.158±0.01	-22.87±0.42	33.89±4.29	9.68±1.23

ATRA, all-trans retinoic acid; EE, encapsulation efficiency rate; DL, drug-loading rate; DLS, dynamic light scattering; PDI, polymer dispersity index.

In vivo antitumor efficacy. The *in vivo* antitumor studies were performed using tumor-bearing BALB/c mice. To mimic the TME, the H22/m-HSC-bearing mice model was established. In the TME, the activated HSCs could promote tumor growth, while the traditional HCC-bearing mouse model was established by subcutaneously injecting H22 cells. Each mouse was subcutaneously injected with 0.2 ml $2x10^6$ H22/m-HSC cells (the ratio of H22 to m-HSC cells was 5:1) or $2x10^6$ H22 cells into the right flank. The anticancer effect of ADHG was studied using these co-implantation mice. When the cancerous volume grew to 150 mm^3, the mice were randomly divided into seven groups (n=5 per group), and free DOX, free ATRA, DOX + ATRA, DH, ADH and ADHG were administrated through the tail vein (equivalent DOX, 3 mg/kg; ATRA, 2.2 mg/kg) while the control group was injected with 0.2 ml of saline. The body weight and tumor volume were detected every other day. The mice were euthanized when they lost 20% of their original body weight or when the tumor volume grew beyond 2,000 mm^3. Mice health and behavior, including activity level, appetite, body temperature, daily behavior, body weight and respiratory rate, were monitored every 2 days. During the experiment, mice were provided with comfortable and clean housing conditions and were checked daily for any abnormal behavior. Mice were anesthetized by intraperitoneal injection of 2% sodium pentobarbital (45 mg/kg) and sacrificed by cervical dislocation when the corneal response had disappeared, the skin pinch response had disappeared and the muscles had relaxed. Following euthanasia, the mice were verified as deceased by checking that the pain response had disappeared and the heartbeat and respiration had stopped. The mice were sacrificed 14 days after drug treatment, and the tumors and major organs were removed for H&E staining, Masson staining and immunohistochemistry assays. Following euthanasia, tumors and major organs were removed and immersed in 4% paraformaldehyde and fixed for 48 h at 4˚C. After the tissue was paraffin-embedded, sections of 4 μm thickness were prepared for H&E staining and immunohistochemistry. The slices were dewaxed in xylene twice for 10 min, followed by rehydration with 100% ethanol twice for 10 min and 95, 80 and 70% ethanol for 5 min each. For H&E staining, hematoxylin staining was performed for 8 min and eosin staining for 2 min at room temperature using an H&E staining kit (cat. no. G1120; Solarbio). Masson staining was performed using a Masson staining kit (cat. no. G1346; Solarbio). For immunohistochemistry, antigen repair by microwave heating at 98˚C for 5 min in citrate buffer solution, permeabilization by 0.1% Triton-100 (cat. no. T8200; Solarbio) for 15 min, endogenous peroxidase blocker (cat. PV-6001; OriGene) at room temperature for 10 min and blocking in 5% albumin bovine V (cat. no. A8020; Solarbio) for 60 min at 37˚C were performed. Samples were incubated with primary antibody at 37˚C for 1 h [α-SMA antibody (cat. no. AF1032; dilution, 1:200; Affinity Biosciences); anti-CD31 antibody (cat. no. ab182981; dilution, 1:2,000; Abcam)]. As secondary antibodies, enzyme-labeled goat anti-rabbit IgG polymer (cat. no. PV-6001; OriGene) was applied for 20 min at room temperature. A DAB color development kit (cat. no. ZLI-9017; OriGene) was used for color development, and counterstaining was performed with hematoxylin for 2 min at room temperature. The microscopy samples were all observed under a light microscope (magnification, x200).

Inhibition of lung metastases. In total, 0.2 ml of $2x10^6$ H22 cells were intravenously injected into the tail vein of BALB/c mice to establish a lung metastasis model. The mice (n=4 per group) were treated via the tail vein with physiological saline (control), free DOX, free ATRA, DOX + ATRA, DH, ADH and ADHG (equivalent DOX, 3 mg/kg; ATRA, 2.2 mg/kg) every 2 days for 14 days. The health of the mice was monitored every 2 days, including activity level, appetite, body temperature, daily behavior, body weight and respiratory rate. Mice were euthanized as described above. Subsequently, the lungs were acquired for H&E staining assay according to the protocol stated above.

Statistical analysis. All statistical analyses were performed using GraphPad Prism 9.0.0 (Dotmatics) and are presented as mean ± SD. All experiments were repeated at least three times. Results were analyzed using one-way or two-way ANOVA followed by Bonferroni's multiple-comparisons test. $P<0.05$ was considered to indicate a statistically significant difference.

Results and discussion

Morphology and characteristics of ADHG nanoparticles. The amphiphilic HA conjugates self-assembled into nano-sized particles. ADHG nanoparticles based on DHG were prepared for co-encapsulating ATRA and DOX, and GA-free co-loaded nanoparticles were named ADH. As shown in Table I, when the ratio of DHG to ATRA was 5:1, the average size of the nanoparticles was 211.95 nm, which was smaller than that of other groups. The DL and EE were 8.79 and 52.72%, respectively. In addition, the morphology of DHG and ADHG were investigated by TEM. In Fig. 1B and C, the dual drug-loaded nanoparticles are shown to be similarly spherical in shape.

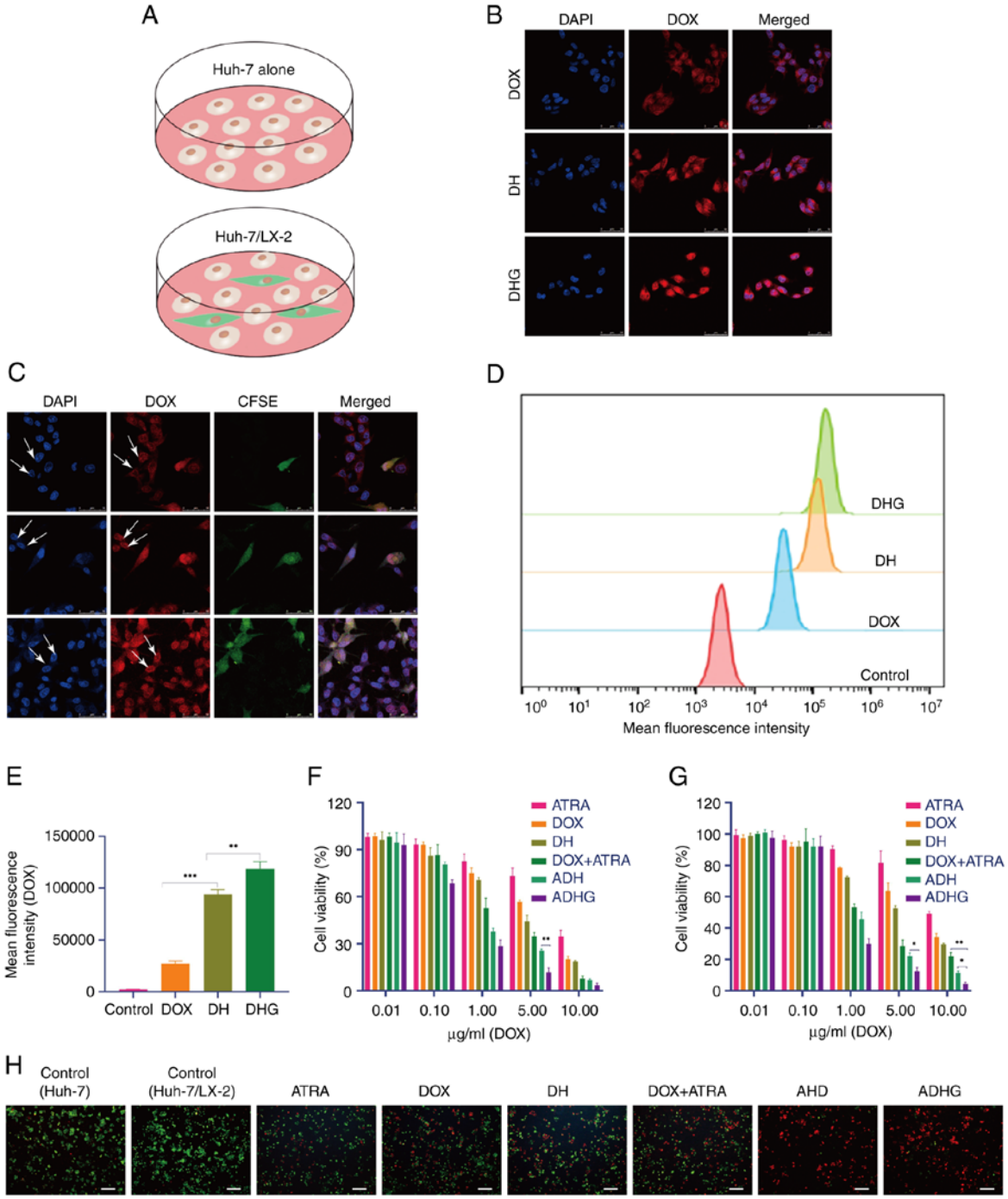

Figure 2. Cellular uptake and cytotoxicity. (A) Two research models used in the present study. Images of (B) Huh-7 cells and (C) the dual-cell model. White arrows indicate the fluorescence intensity of Huh-7 cells. (D) Flow cytometry assay and (E) its quantitative analysis. Cytotoxicity of (F) Huh-7 cells alone and (G) the dual-cell model. (H) Live/dead staining test (scale bar, 100 μm). *P<0.05, **P<0.01 and ***P<0.001. DHG, DOX-sHA-GA; DH, DOX-sHA; DOX, doxorubicin; CFSE, 5(6)-carboxyfluorescein diacetate succinimidyl ester; ATRA, all-trans retinoic acid; ADH, ATRA/DOX-sHA; ADHG, ATRA/DOX-sHA-GA; sHA, sulfated hyaluronic acid.

To evaluate the stability of the nano-delivery system, the characteristics of ADHG were measured for 7 days. Fig. 1D and E shows that no notable changes were observed in particle size and zeta potential within 7 days, suggesting that ADHG nanoparticles were stable under physiological conditions.

Cellular uptake and cytotoxicity assay. In the TME, stromal cells, such as HSCs, have been proven to facilitate cancer development (36). To simulate the TME, a dual-cell research model was established by mixing HSCs and HCC cells together, while HCC cells alone were used as the control (Fig. 2A).

The cellular uptake of ADHG was detected in HCC cells, in which red fluorescence (DOX) tracked the intracellular drug distribution, and blue fluorescence (DAPI) indicated nuclear location. Considering that GA receptors are highly expressed in liver cancer cells, DHG nanoparticles were prepared for co-delivery of DOX and ATRA. As shown in Fig. 2B, compared with ADH, there was more red fluorescence signal

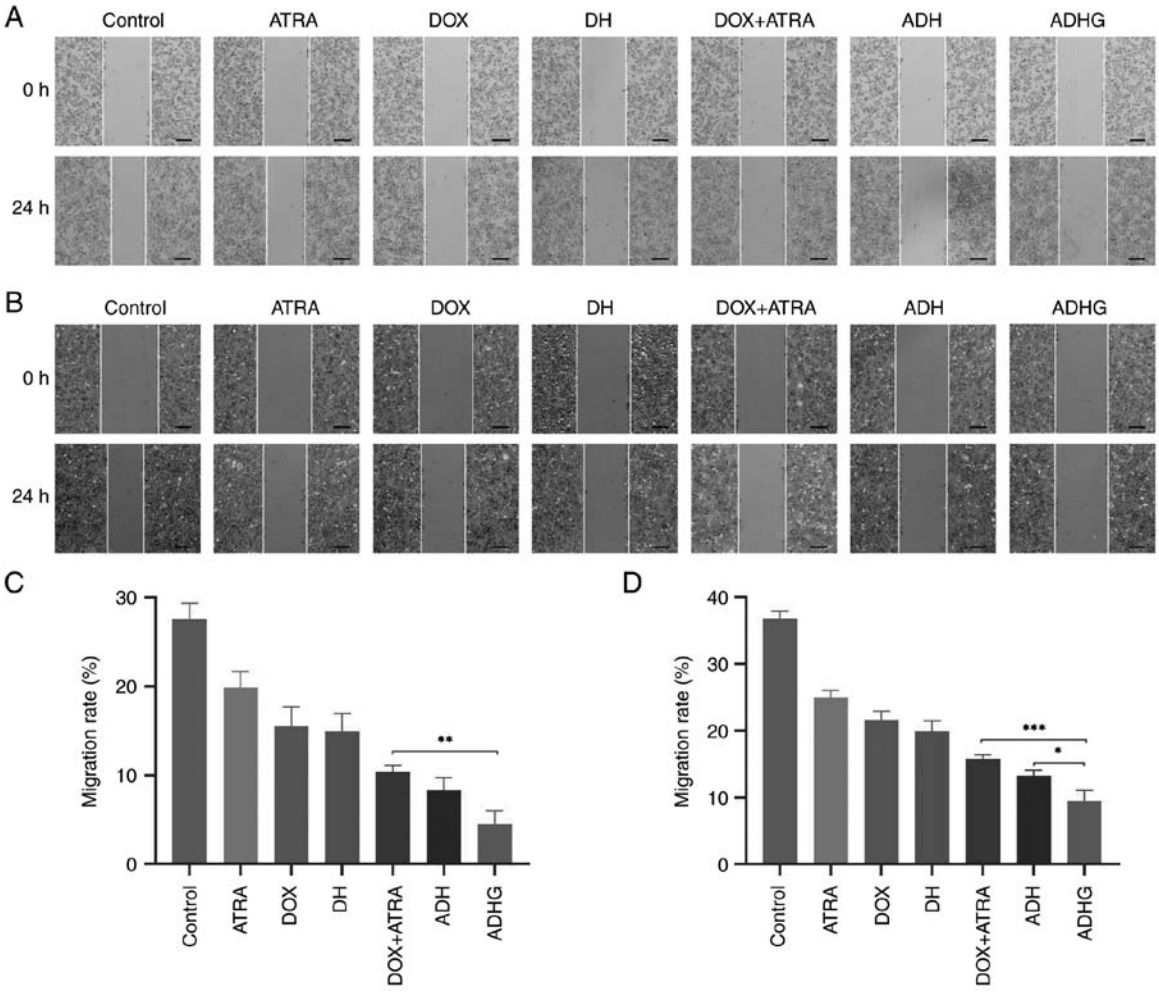

Figure 3. Anti-migration effect of ADHG. Wound-healing assay using (A) Huh-7 cells alone and (B) the dual-cell research model (scale bar, 100 μm). Migration rates of (C) Huh-7 cells alone and (D) the dual-cell model. The experiment was performed in triplicate. *P<0.05, **P<0.01 and ***P<0.001. ATRA, all-trans retinoic acid; ADH, ATRA/DOX-sHA; ADHG, ATRA/DOX-sHA-GA; DOX, doxorubicin; DH, DOX-sHA; sHA, sulfated hyaluronic acid.

in the cells treated with ADHG. One possible explanation for this is that the GA ligand promoted ADHG internalization via GA/GA receptor-mediated endocytosis.

In fact, the HCC-HSCs interaction has been shown to facilitate cancer development; hence, targeting both HSCs and tumor cells might be a potential anticancer strategy. In the present study, a dual-cell model was established in which HSCs were marked with CFSE dye. In Fig. 2C, strong red fluorescence was observed in both HSCs and Huh-7 cells, indicating that the drug was taken up by the cells. Considering that the CD44 protein is highly expressed on HSCs (37), ADHG might have been taken up by HSCs and Huh-7 cells through HA/CD44- and GA/GA receptor-mediated internalization, respectively. This result was also confirmed by FCM (Fig. 2D and E), in which more drugs were detected in the cells treated with ADHG.

In the present study, MTT assays were performed on HCC cells and the dual-cell model. In Fig. 2F and G, all drug-treated groups exhibited dose-dependent cytotoxicity. Of note, the dual-drug groups exhibited a greater inhibitory effect than single-drug groups, suggesting that the combined treatment of DOX and ATRA enhanced the antitumor effect. As expected, ADHG had lower cell viability than the other groups. Since ATRA were modified by the GA ligand, it is indicated that GA/GA receptor-mediated drug internalization promoted apoptosis.

Similarly, the cytotoxicity of ADHG in the dual-cell model was detected by MTT assay. On note, the IC_{50} of free DOX was 6.627 μg/ml, which was 1.8-fold of that in Huh-7 cells alone. This result suggested that HSCs might induce drug resistance of the tumor cells in the dual-cell model. In fact, it has been shown that cancer cells exist in a complex TME, in which HSCs have a vital role in cancer development through the HSC-cancer cell interaction (38). Hence, the dual-cell research model was an appropriate model for anticancer studies *in vitro*. Furthermore, in the two nano-sized drug groups, particularly ADHG, higher cytotoxicity was observed than in the DOX + ATRA group. Live/dead staining (Fig. 2H) was further performed on the dual-cell model. Of note, more red-stained cells (dead cells) were observed in the ADHG group, indicating that ADHG was able to efficiently constrain cancer cell proliferation in the presence of HSCs.

Wound-healing assay. To examine the anti-migration efficacy of ADHG nanoparticles, a wound-healing assay was performed on the HCC (Huh-7) cells (Fig. 3A). However, it has been shown that HSCs can promote tumor migration

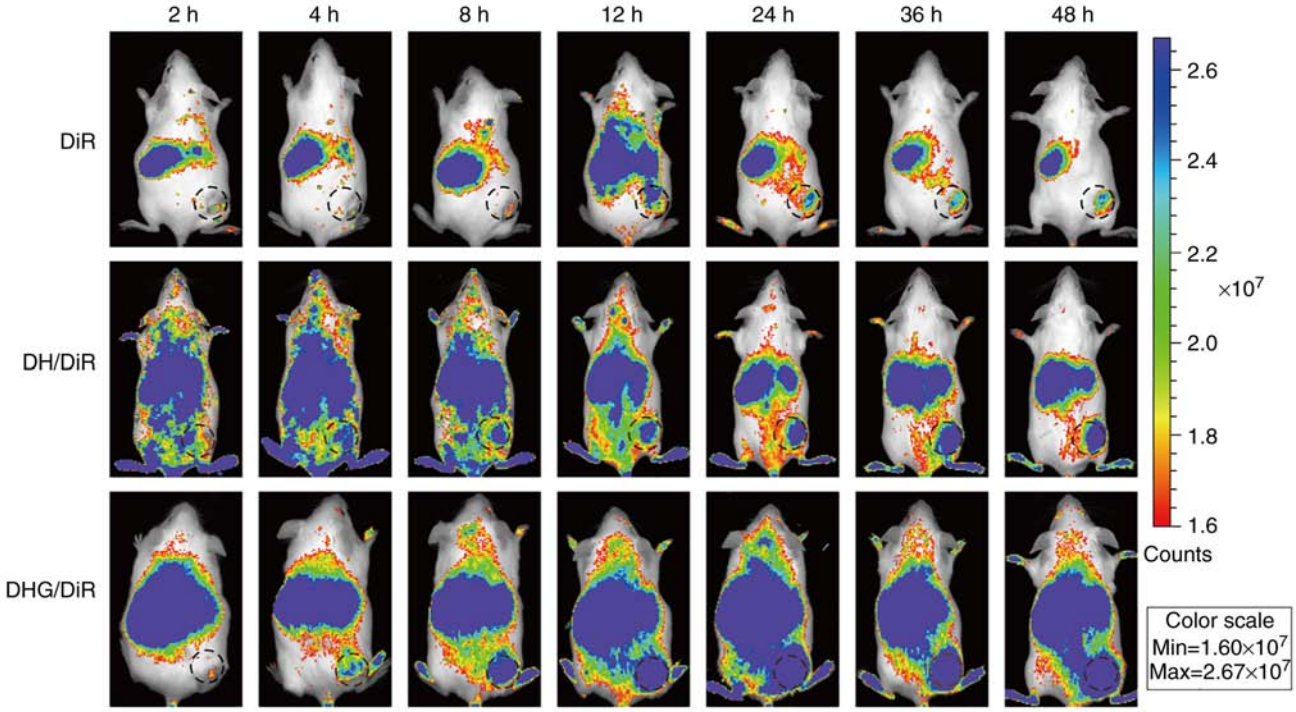

Figure 4. *In vivo* drug distribution in subcutaneous tumor-bearing mice. DiR fluorescence imaging of DiR, DH/DiR and DHG/DiR in 0-48 h. DiR, 1,1-dioctadecyl-3,3,3,3-tetramethylindotricarbocyanine iodide; DH, doxorubicin-sulfated hyaluronic acid; DHG, doxorubicin-sulfated hyaluronic acid-glycyrrhetinic acid.

by secreting numerous pro-migration factors (39). To simulate the TME, a dual-cell model composed of Huh-7 and CFSE-labeled HSCs was established (Fig. 3B). Compared with the control, different drug formulations had inhibitory effects on cell migration in Huh-7 cells (Fig. 3C). As expected, ADHG treatment inferred a lower migration rate in comparison with ADH or DOX + ATRA, suggesting that the nano-sized therapeutic combination approach could promote anti-migration efficacy.

Interestingly, in Fig. 3D, the migration rate in the dual-cell model (36.75%) was higher than in Huh-7 cells alone (27.55%) in the control group, suggesting that HSCs facilitated the migration of Huh-7 cells. ADHG resulted in a greater inhibitory effect than other drug formulations, indicating that the proliferation and migration of HCC could be effectively restrained by the nano-sized combination therapy based on DHG conjugates.

In vivo imaging experiments. To investigate the cancer-targeting property of DHG nanoparticles, DiR-loaded nanoparticles were prepared and injected into tumor-bearing mice. Fig. 4 shows that the fluorescent signals of free DiR groups in the tumor area reached their peak at 12 h, then notably decreased. Compared with the control, the dual drug-loaded nanoparticles showed stronger fluorescence in the cancer region. A possible explanation is that the nano-sized vehicles could accumulate in the tumor due to enhanced permeability and retention effects (40,41). As expected, the fluorescence intensity of the DHG + DiR group was higher than that of DH + DiR at 48 h, suggesting that the GA ligand promoted drug internalization in cancer cells.

In vivo antitumor effect against HCC/HSC co-implanted mice. In the TME, the activated HSCs could promote tumor growth, while the traditional HCC-bearing mouse model was established by subcutaneously injecting H22 cells alone. To simulate the TME, an *in vivo* HCC/HSC-bearing mice model was established to examine the anticancer effect of ADHG (Fig. 5A). In a previous study, by our group the DOX-loaded formulation at 3 mg/kg could inhibit HCC development (42). Hence, in the present study, 3 mg/kg of DOX was chosen for the *in vivo* antitumor studies. In the present study, 5 mice in the co-implantation control 2 group reached the humane endpoint on day 11, with tumor volumes exceeding 2,000 mm^3, and these 5 mice were euthanized. Of note, compared with the traditional H22 tumor-bearing mice model (control 1, saline), the cancerous volume in the co-implantation model (control 2, saline) was greater (Fig. 5B and C). Since HSCs are located in the TME, HCC/HSC-bearing mice are a more appropriate model than HCC-bearing model for anti-hepatoma studies. After 14 days, cancer progression was constrained in all drug-treated groups. Similar to the *in vitro* results, the dual-drug groups exhibited smaller tumor sizes than the single-drug groups, suggesting that ATRA promoted a DOX-induced anti-proliferative effect. Moreover, the inhibition rate of the ADHG group was 85.8%, which was higher than that in the DOX + ATRA (67.9%) or ADH (76.0%) groups (Fig. 5D). The anti-proliferative assay result was also confirmed by the results of the H&E assay, in which severe apoptosis was observed in the ADHG group (Fig. 5E). One explanation may be that ADHG was internalized by the cancer cells and HSCs in an active-targeting manner (HA/CD44 and/or GA/GA receptor-mediated endocytosis), resulting in a greater inhibitory effect.

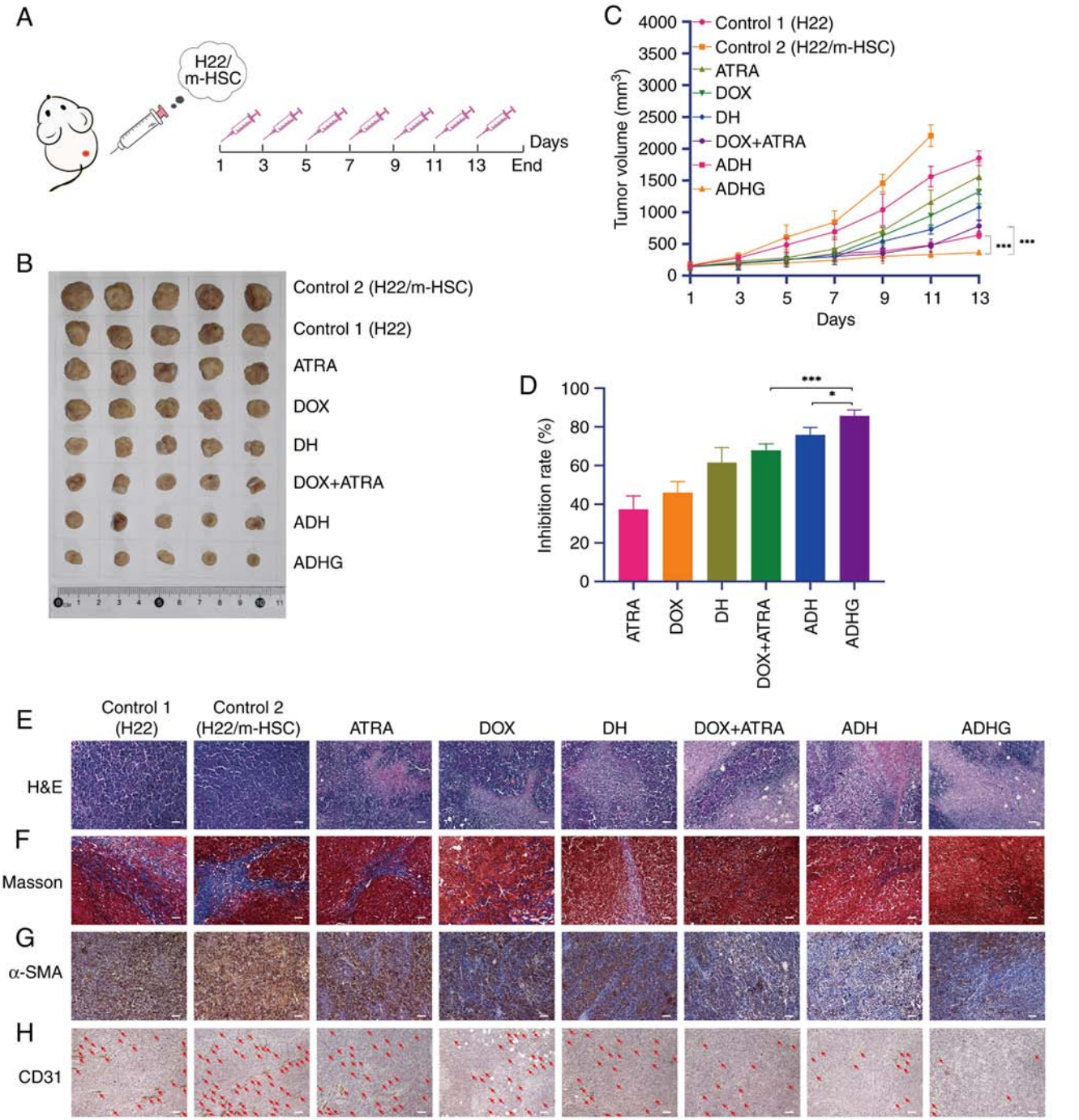

Figure 5. Evaluation of anti-hepatoma activity in H22/m-HSC-bearing mice. (A) Treatment schedule. (B) Tumor images. (C) Tumor volumes. (D) Tumor growth inhibition rates. (E) H&E and (F) Masson staining assays. Immunohistochemical assays of (G) α-SMA and (H) CD31 proteins, with red arrows indicating the tumor vessels (scale bars, 50 μm). *P<0.05 and ***P<0.001. m-HSC, mouse hepatic stellate cells; SMA, smooth muscle actin; ATRA, all-trans retinoic acid; ADH, ATRA/DOX-sHA; ADHG, ATRA/DOX-sHA-GA; DOX, doxorubicin; DH, DOX-sHA; sHA, sulfated hyaluronic acid.

In addition, Masson staining and immunohistochemistry assays were conducted to further investigate the anticancer effect of ADHG. Studies have revealed that activated HSCs have an important role in ECM deposition by secreting collagen fibers (43,44). Fig. 5F indicated that the blue-colored region (collagen fiber) was larger in Control 2 (H22/m-HSC) than that in Control 1 (H22), which may be due to HSC activation. By contrast, there was almost no blue-colored area in the ADHG group indicating negative ECM deposition. In Fig. 5G, a notable α-SMA^{+} region was present in Control 2 (H22/m-HSCS), suggesting that activated HSCs were distributed in the cancerous tissues. Furthermore, the α-SMA^{+} region was decreased in the ADHG group, indicating that ADHG could block HSC activation, resulting in lower ECM deposition. In addition, it has been proven that tumor angiogenesis may promote tumor proliferation and metastasis (45,46). The platelet endothelial cell adhesion molecule CD31, a marker of blood vessels, was used to examine angiogenesis. In Fig. 5H, compared with the other drug-treated groups, there were fewer vessels in the ADHG group, indicating that ADHG

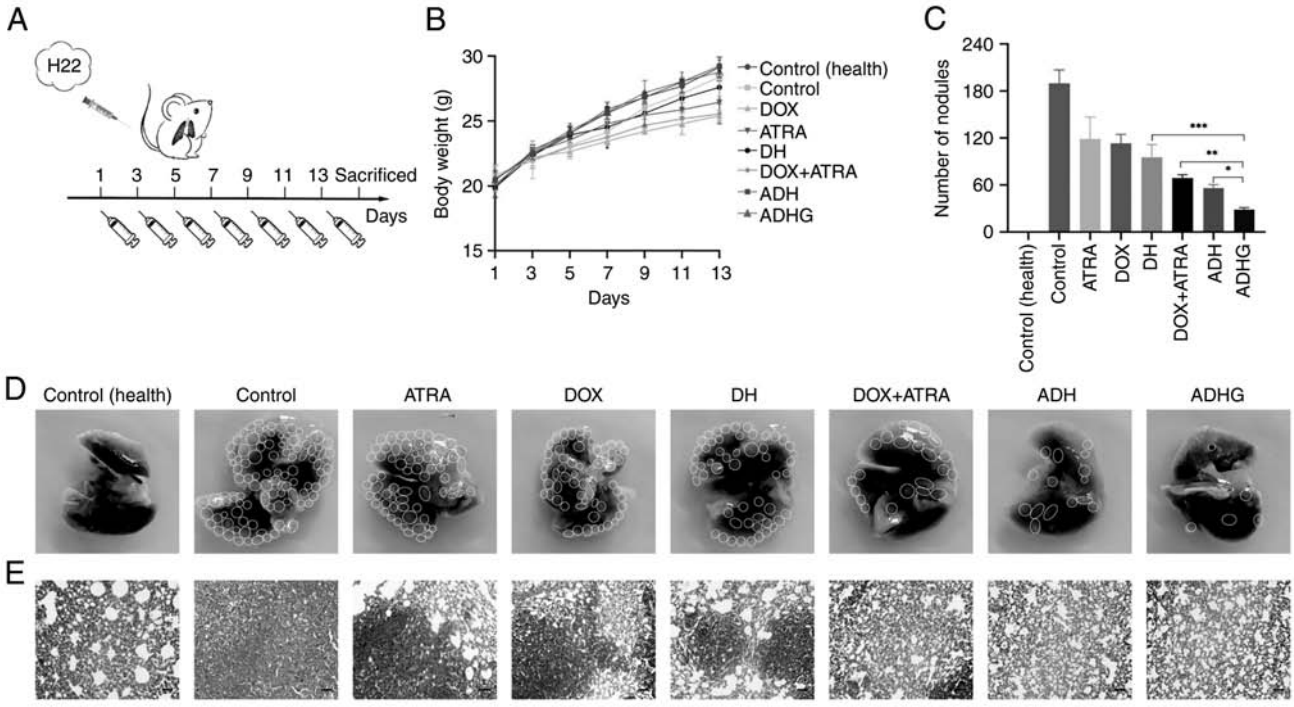

Figure 6. Evaluation of the anti-metastatic effect of ADHG. (A) Model establishment and drug administration. (B) Mice weight over time. (C) Quantitative analysis of metastatic nodules. (D) Lung images; circles indicate transfer areas of tumor metastasis. (E) H&E analysis (magnification, x200). *P<0.05, **P<0.01 and ***P<0.001. ATRA, all-trans retinoic acid; ADH, ATRA/DOX-sHA; ADHG, ATRA/DOX-sHA-GA; DOX, doxorubicin; DH, DOX-sHA; sHA, sulfated hyaluronic acid.

was able to inhibit tumor angiogenesis. Hence, the combined therapeutic design based on HA polymers could suppress HSCs-HCC interaction and constrain HCC progression.

In vivo suppression of lung metastasis. Mice with lung metastases were established to examine the anti-metastatic effect of ADHG (Fig. 6A). Considering that the metastatic nodules in the lungs were very small, it was difficult to monitor the progression of internal tumors in real-time. According to previous lung metastasis studies (47,48), the lung tissues were harvested to evaluated the anti-metastasis effect of different drug groups. Similar to the anti-proliferation evaluation *in vivo*, no significant differences in mice weight were observed between the healthy control and the nanoparticle-treated mice (Fig. 6B). Notably, numerous metastatic nodules occurred in the control model (Fig. 6C and D), and the dual-drug treatment groups contained fewer metastatic nodules than the free DOX group, indicating that ATRA improved the anti-metastatic effect of DOX. Notably, the ADHG group presented the smallest number of nodules among all drug-treated groups. This result was consistent with the H&E assay. Fig. 6E showed that no notable tumor regions were observed in the lungs of the mice treated with ADHG. These results may be due to the fact that ADHG could be taken up by metastatic HCC cells, resulting in an enhanced anti-proliferative and anti-metastatic effect.

Conclusion. In summary, DHG conjugates were synthesized for co-delivery of ATRA and DOX for anti-HCC therapy, and HCC/HSC research models were established for the *in vitro* and the *in vivo* anti-HCC studies. The results showed that ADHG nanoparticles were spherical in shape with high stability and were readily taken up by HSCs and HCC cells simultaneously. Compared with free DOX, ATRA increased the inhibitory effect on tumor proliferation and migration. The *in vivo* biodistribution images indicated that DHG nanoparticles accumulated in the tumor region. The *in vivo* anticancer results showed that, compared with other groups, ADHG nanoparticles exhibited lower ECM deposition, less tumor angiogenesis and stronger pro-apoptotic and anti-metastatic effects. However, further studies are needed to explore the anti-tumor mechanisms of ADHG nanoparticles, and there are still many difficulties to overcome in terms of clinical applications.

Acknowledgements

Not applicable.

Funding

This work was supported by the National Science Foundation of China (grant no. 81803464), the Sci-Technology Development Program of Weifang (grant no. 2021GX053) and Scientific Research Project of Weifang University of Science and Technology (grant nos. 2021XKJS12 and 2021XKJS19).

Availability of data and materials

The datasets used and/or analyzed in the current study are available from the corresponding author on reasonable request.

Authors' contributions

JW designed the experiments. QL, XG and GJ performed the antitumor studies and drafted the manuscript. SL performed the *in vitro* and *in vivo* mouse model experiments. KS and GT analyzed the data. GT and SL confirm the authenticity of all the raw data. JW edited the manuscript. All authors have read and approved the final version manuscript.

Ethics approval and consent to participate

The present study was approved by the Animal Ethics Committee of Weifang Medical University (Weifang, China; approval no. 2019SDL045).

Patient consent for publication

Not applicable.

Competing interests

The authors declare that they have no competing interests.

References

1. Lee YS and Jeong WI: Retinoic acids and hepatic stellate cells in liver disease. J Gastroenterol Hepatol 27 (Suppl 2): S75-S79, 2012.
2. Hisamori S, Tabata C, Kadokawa Y, Okoshi K, Tabata R, Mori A, Nagayama S, Watanabe G, Kubo H and Sakai Y: All-trans-retinoic acid ameliorates carbon tetrachloride-induced liver fibrosis in mice through modulating cytokine production. Liver Int 28: 1217-1225, 2008.
3. Mizobuchi Y, Shimizu I, Yasuda M, Hori H, Shono M and Ito S: Retinyl palmitate reduces hepatic fibrosis in rats induced by dimethylnitrosamine or pig serum. J Hepatol 29: 933-943, 1998.
4. Davis BH, Kramer RT and Davidson NO: Retinoic acid modulates rat Ito cell proliferation, collagen, and transforming growth factor beta production. J Clin Invest 86: 2062-2070, 1990.
5. Tsuchida T and Friedman SL: Mechanisms of hepatic stellate cell activation. Nat Rev Gastroenterol Hepatol 14: 397-411, 2017.
6. Panebianco C, Oben JA, Vinciguerra M and Pazienza V: Senescence in hepatic stellate cells as a mechanism of liver fibrosis reversal: A putative synergy between retinoic acid and PPAR-gamma signalings. Clin Exp Med 17: 269-280, 2017.
7. Wang L, Tankersley LR, Tang M, Potter JJ and Mezey E: Regulation of the murine alpha(2)(I) collagen promoter by retinoic acid and retinoid X receptors. Arch Biochem Biophys 401: 262-270, 2002.
8. Kim SJ, Park JH, Lee SA, Lee JG, Shin JM and Lee HM: All-trans retinoic acid regulates TGF-β1-induced extracellular matrix production via p38, JNK, and NF-κB-signaling pathways in nasal polyp-derived fibroblasts. Int Forum Allergy Rhinol 10: 636-645, 2020.
9. Zhang Y, Guan DX, Shi J, Gao H, Li JJ, Zhao JS, Qiu L, Liu J, Li N, Guo WX, *et al*: All-trans retinoic acid potentiates the chemotherapeutic effect of cisplatin by inducing differentiation of tumor initiating cells in liver cancer. J Hepatol 59: 1255-1263, 2013.
10. Abu Lila AS and Ishida T: Liposomal delivery systems: Design optimization and current applications. Biol Pharm Bull 40: 1-10, 2017.
11. Li L and Wang H: Heterogeneity of liver cancer and personalized therapy. Cancer Lett 379: 191-197, 2016.
12. Wu T and Dai Y: Tumor microenvironment and therapeutic response. Cancer Lett 387: 61-68, 2017.
13. Han S, Wang W, Wang S, Yang T, Zhang G, Wang D, Ju R, Lu Y, Wang H and Wang L: Tumor microenvironment remodeling and tumor therapy based on M2-like tumor associated macrophage-targeting nano-complexes. Theranostics 11: 2892-2916, 2021.
14. Hui L and Chen Y: Tumor microenvironment: Sanctuary of the devil. Cancer Lett 368: 7-13, 2015.
15. Mohr R, Özdirik B, Lambrecht J, Demir M, Eschrich J, Geisler L, Hellberg T, Loosen SH, Luedde T, Tacke F, *et al*: From liver cirrhosis to cancer: The role of Micro-RNAs in hepatocarcinogenesis. Int J Mol Sci 22: 1492, 2021.
16. Brodt P: Role of the microenvironment in liver metastasis: From pre- to prometastatic niches. Clin Cancer Res 22: 5971-5982, 2016.
17. Muppala S: Significance of the tumor microenvironment in liver cancer progression. Crit Rev Oncog 25: 1-9, 2020.
18. Kahn AM, Blenman KRM, Sonis ST and Lustberg MB: Strategies to mitigate the toxicity of cancer therapeutics. Adv Cancer Res 155: 215-244, 2022.
19. Zhou F, Teng F, Deng P, Meng N, Song Z and Feng R: Recent progress of nano-drug delivery system for liver cancer treatment. Anticancer Agents Med Chem 17: 1884-1897, 2018.
20. Sun D, Zhang J, Wang L, Yu Z, O'Driscoll CM and Guo J: Nanodelivery of immunogenic cell death-inducers for cancer immunotherapy. Drug Discov Today 26: 651-662, 2021.
21. Sudha PN and Rose MH: Beneficial effects of hyaluronic acid. Adv Food Nutr Res 72: 137-176, 2014.
22. Vasvani S, Kulkarni P and Rawtani D: Hyaluronic acid: A review on its biology, aspects of drug delivery, route of administrations and a special emphasis on its approved marketed products and recent clinical studies. Int J Biol Macromol 151: 1012-1029, 2020.
23. Lokeshwar VB, Mirza S and Jordan A: Targeting hyaluronic acid family for cancer chemoprevention and therapy. Adv Cancer Res 123: 35-65, 2014.
24. Benitez A, Yates TJ, Lopez LE, Cerwinka WH, Bakkar A and Lokeshwar VB: Targeting hyaluronidase for cancer therapy: Antitumor activity of sulfated hyaluronic acid in prostate cancer cells. Cancer Res 71: 4085-4095, 2011.
25. Jordan AR, Lokeshwar SD, Lopez LE, Hennig M, Chipollini J, Yates T, Hupe MC, Merseburger AS, Shiedlin A, Cerwinka WH, *et al*: Antitumor activity of sulfated hyaluronic acid fragments in pre-clinical models of bladder cancer. Oncotarget 8: 24262-24274, 2017.
26. Zhou X, He C, Liu M, Chen Q, Zhang L, Xu X, Xu H, Qian Y, Yu F, Wu Y, *et al*: Self-assembly of hyaluronic acid-mediated tumor-targeting theranostic nanoparticles. Biomater Sci 9: 2221-2229, 2021.
27. Bai Y, Liu CP, Chen D, Liu CF, Zhuo LH, Li H, Wang C, Bu HT and Tian W: β-Cyclodextrin-modified hyaluronic acid-based supramolecular self-assemblies for pH- and esterase-dual-responsive drug delivery. Carbohydr Polym 246: 116654, 2020.
28. Cai J, Fu J, Li R, Zhang F, Ling G and Zhang P: A potential carrier for anti-tumor targeted delivery-hyaluronic acid nanoparticles. Carbohydr Polym 208: 356-364, 2019.
29. Lei C, Liu XR, Chen QB, Li Y, Zhou JL, Zhou LY and Zou T: Hyaluronic acid and albumin based nanoparticles for drug delivery. J Control Release 331: 416-433, 2021.
30. Du W, Yang X, He S, Wang J, Guo Y, Kou B, Jiang Y, Bian P, Li B and Yin L: Novel hyaluronic acid oligosaccharide-loaded and CD44v6-targeting oxaliplatin nanoparticles for the treatment of colorectal cancer. Drug Deliv 28: 920-929, 2021.
31. Lai H, Ding X, Ye J, Deng J and Cui S: pH-responsive hyaluronic acid-based nanoparticles for targeted curcumin delivery and enhanced cancer therapy. Colloids Surf B Biointerfaces 198: 111455, 2021.
32. Nieto C, Vega MA and Martín Del Valle E: Nature-inspired nanoparticles as paclitaxel targeted carrier for the treatment of HER2-positive breast cancer. Cancers (Basel) 13: 2526, 2021.
33. Silva EL, Carneiro G, Caetano PA, Goulart G, Ferreira Costa D, de Souza-Fagundes EM, Gomes DA and Ferreira LA: Nanostructured lipid carriers loaded with tributyrin as an alternative to improve anticancer activity of all-trans retinoic acid. Expert Rev Anticancer Ther 15: 247-256, 2015.
34. Xu ZC, Shen HX, Chen C, Ma L, Li WZ, Wang L and Geng ZM: Neuropilin-1 promotes primary liver cancer progression by potentiating the activity of hepatic stellate cells. Oncol Lett 15: 2245-2251, 2018.
35. Justus CR, Leffler N, Ruiz-Echevarria M and Yang LV: In vitro cell migration and invasion assays. J Vis Exp 88: 51046, 2014.
36. Bourebaba N and Marycz K: Hepatic stellate cells role in the course of metabolic disorders development-A molecular overview. Pharmacol Res 170: 105739, 2021.
37. Gu L, Zhang F, Wu J and Zhuge Y: Nanotechnology in drug delivery for liver fibrosis. Front Mol Biosci 8: 804396, 2022.
38. Hellerbrand C: Hepatic stellate cells-the pericytes in the liver. Pflugers Arch 465: 775-778, 2013.

39. Iwahasi S, Rui F, Morine Y, Yamada S, Saito YU, Ikemoto T, Imura S and Shimada M: Hepatic stellate cells contribute to the tumor malignancy of hepatocellular carcinoma through the IL-6 pathway. Anticancer Res 40: 743-749, 2020.
40. Maeda H, Wu J, Sawa T, Matsumura Y and Hori K: Tumor vascular permeability and the EPR effect in macromolecular therapeutics: A review. J Control Release 65: 271-284, 2000.
41. Shi Y, van der Meel R, Chen X and Lammers T: The EPR effect and beyond: Strategies to improve tumor targeting and cancer nanomedicine treatment efficacy. Theranostics 10: 7921-7924, 2020.
42. Li Z, Wang F, Li Y, Wang X, Lu Q, Wang D, Qi C, Li C, Li Z, Lian B, *et al*: Combined anti-hepatocellular carcinoma therapy inhibit drug-resistance and metastasis via targeting 'substance P-hepatic stellate cells-hepatocellular carcinoma' axis. Biomaterials 276: 121003, 2021.
43. Meng Q, Luo X, Chen J, Wang D, Chen E, Zhang W, Zhang G, Zhou W, Xu J and Song Z: Unmasking carcinoma-associated fibroblasts: Key transformation player within the tumor microenvironment. Biochim Biophys Acta Rev Cancer 1874: 188443, 2020.
44. Fiori ME, Di Franco S, Villanova L, Bianca P, Stassi G and De Maria R: Cancer-associated fibroblasts as abettors of tumor progression at the crossroads of EMT and therapy resistance. Mol Cancer 18: 70, 2019.
45. Li T, Kang G, Wang T and Huang H: Tumor angiogenesis and anti-angiogenic gene therapy for cancer. Oncol Lett 16: 687-702, 2018.
46. Bhat SM, Badiger VA, Vasishta S, Chakraborty J, Prasad S, Ghosh S and Joshi MB: 3D tumor angiogenesis models: Recent advances and challenges. J Cancer Res Clin Oncol 147: 3477-3494, 2021.
47. Wang Y, Xu Z, Guo S, Zhang L, Sharma A, Robertson GP and Huang L: Intravenous delivery of siRNA targeting CD47 effectively inhibits melanoma tumor growth and lung metastasis. Mol Ther 21: 1919-1929, 2013.
48. Chen Q, Bai H, Wu W, Huang G, Li Y, Wu M, Tang G and Ping Y: Bioengineering bacterial vesicle-coated polymeric nanomedicine for enhanced cancer immunotherapy and metastasis prevention. Nano Lett 20: 11-21, 2020.